Journal Pre-proof

Where to build the ideal solar-powered ammonia plant? Design optimization of a Belgian and Moroccan power-to-ammonia plant for covering the Belgian demand under uncertainties

Kevin Verleysen, Diederik Coppitters, Alessandro Parente, Francesco Contino

PII: S2666-352X(23)00030-4
DOI: https://doi.org/10.1016/j.jaecs.2023.100141
Reference: JAECS 100141

To appear in: *Applications in Energy and Combustion Science*

Received date : 9 December 2022
Revised date : 5 April 2023
Accepted date : 5 May 2023

Please cite this article as: K. Verleysen, D. Coppitters, A. Parente et al., Where to build the ideal solar-powered ammonia plant? Design optimization of a Belgian and Moroccan power-to-ammonia plant for covering the Belgian demand under uncertainties. *Applications in Energy and Combustion Science* (2023), doi: https://doi.org/10.1016/j.jaecs.2023.100141.

Where to build the ideal solar-powered ammonia plant? Design optimization of a Belgian and Moroccan power-to-ammonia plant for covering the Belgian demand under uncertainties.

Kevin Verleysen[a,b,c,*], Diederik Coppitters[d], Alessandro Parente[b,c], Francesco Contino[d]

[a] *Thermo and Fluid Dynamics (FLOW), Vrije Universiteit Brussel (VUB), Pleinlaan 2, 1050 Brussels, Belgium*
[b] *Aéro-thermo-mécanique (ATM), Université Libre de Bruxelles (ULB), Avenue F.D. Roosevelt, 50 - CP 165/41, 1050 Brussels, Belgium*
[c] *Brussels Institute for Thermal-fluid systems and clean Energy (BRITE), Vrije Universiteit Brussel (VUB) and Université Libre de Bruxelles (ULB), 1050 Brussels, Belgium*
[d] *Institute of Mechanics, Materials and Civil Engineering (iMMC), Université Catholique de Louvain (UCLouvain), Place du Levant, 2, 1348 Louvain-la-Neuve*

Abstract

Regions with abundantly available renewable energy are not necessarily the same as those with a high population density and energy consumption. Therefore, renewable energy can be produced in optimal climate conditions with a remote renewable hub and transported to these population-dense regions. To establish this energy transport to these regions, ammonia provides a flexible, easy-to-handle energy carrier. However, current literature rarely considers the impact of techno-economic uncertainty on the feasibility of this transport. Using those uncertainties, we performed a robust design optimization on the levelized cost of ammonia and the power-to-ammonia efficiency to compare the local (Belgium) and remote (Morocco) ammonia production and transport to Belgium. This paper provides the robust designs (i.e. least sensitive to uncertainty) for local and remote renewable ammonia production and the advantages of both approaches on the levelized cost and energy efficiency. The results confirm that ammonia production in regions with high solar irradiance followed

*Corresponding author
Email address: kevin.verleysen@vub.be (Kevin Verleysen)

by the transport of ammonia is cost-effective and robust (601 euro/tonne$_{NH_3}$ in mean and 98 euro/tonne$_{NH_3}$ in standard deviation) over local production (852 euro/tonne$_{NH_3}$ in mean and 139 euro/tonne$_{NH_3}$ in standard deviation). However, local ammonia production provides for more efficient (54.8% in mean) and less sensitive power-to-ammonia plant designs (0.16% in standard deviation), while the production in Morocco is less efficient (52.2% in mean) and more sensitive to uncertainties (0.39% in standard deviation). The capacity of the photovoltaic arrays and the electrolyzers highly influences both objectives. The sensitivity analysis shows that capital and operational expenses of the photovoltaics and electrolyzer stack dominate the designs with the lowest levelized cost in mean and standard deviation. However, the energy consumption uncertainty of the Haber-Bosch also impacts the cost of the lowest mean levelized cost. This uncertainty also dominates the designs with the highest energy efficiency in mean and lowest standard deviation.

Keywords: Power-to-ammonia, Haber-Bosch Synthesis, Robust design optimization, Uncertainty quantification, Levelized cost of ammonia

1. Introduction

Ammonia (NH_3) as an energy carrier boomed in recent years because it can support the defossilisation of the energy industry [1]. Producing this energy carrier in large mass is becoming increasingly important for transporting renewable-based hydrogen (H_2) over large distances. In addition, the transition towards renewable NH_3 helps to advance from a fossil-fueled production of nitrogen (N_2) fertilizers to their renewable counterparts [2–4]. In 2020, Belgium imported 1010 ktonne of NH_3 while locally producing 990 ktonne of NH_3 [5] which corresponds to 11.9% of Europe's NH_3 production and 0.79% of the global NH_3 production [6]. This consumption is mainly driven by the Belgian fertilizer industry (production of nitrogen-based fertilizers) and the use of nitrogen fertilizers in the European agricultural sector. In the future, NH_3 could have a wide range of applications similar to renewable H_2, such as becoming an alter-

native maritime fuel or being used in the power industry in combination with gas turbines [7]. Projects worldwide (between Japan and Australia, in Germany and Korea) examine the advantage of renewable NH_3 and its possibility of transporting this energy vector via ship or pipelines to other neighboring countries or continents [8]. For instance, the consortium with Australian and Japanese member industries wants to establish the production and transportation of cheap renewable NH_3 from energy-rich locations to high-demand locations. Other projects are looking for ways to use this NH_3 as a direct or indirect fuel for producing electricity [7]. In the case of Belgium, renewable energy sources are scarce compared to other regions in Europe with higher wind speed (e.g. north of Scotland) and solar irradiance (e.g. south Europe) [9]; therefore, Belgium can not rely only on domestic renewable energy supply in the future [10]. The study of Limpens et al. [11] already showed the drive toward Power-to-Gas (PtG) systems to compensate for the need for seasonal storage and flexibility in a low-CO_2 emission society. The hydrogen import coalition showed the economic feasibility of importing renewable energy to Belgium overseas through the use of energy carriers [12]. These energy carriers included H_2, NH_3, methane (CH_4), methanol (CH_3OH) and liquid organic hydrogen carriers. The report observed that producing NH_3 and CH_3OH in Chile, Oman and Morocco were competitive against different hydrogen production sites in Belgium [12]. Another advantage of considering import over local NH_3 production is the additional electric load on the electricity grid when renewables are insufficient to cover the Power-to-NH_3 ($PtNH_3$) system baseload [13]. Although this local production would be favorable—there is no need for long-distance transport—$PtNH_3$ plants in northern Africa can be beneficial because of the more suitable location in terms of availability of water and high solar irradiance, than in Belgium, which has a population-dense coast and low solar irradiance [2, 8, 12].

The transition from the fossil-fueled Haber-Bosch (HB) plant to the renewable-powered $PtNH_3$ one is encouraged to reduce the global carbon footprint of nitrogen fertilizers and to cover the future energy demand [14–16]. The traditional HB process must operate at a steady-state condition at its nominal conditions.

With a typical HB process, $PtNH_3$ plants would require, in practice, large H_2 tanks and a backup system to continue the NH_3 production. This setup is needed to ensure continuous production when powered by intermittent renewable energy in remote locations [8, 17, 18]. The need for large-scale intermediate storage is highlighted in the work of Osman et al. [19], where the Levelized Cost Of Ammonia (LCOA) was optimized for a steady-state solar-powered $PtNH_3$ plant. To acquire a continuous NH_3 production of 1840 $\mathrm{tonne_{NH_3}/day}$ throughout the year, the NH_3 plant requires a photovoltaic array capacity of 2.54 $\mathrm{GW_p}$, an electrolyzer capacity of 1.44 GW, 2.26 GWh of battery storage and 23.6 GWh of H_2 storage. This battery capacity has not been realized in practice, e.g. the Alamitos Energy Storage project in California is currently pursuing a battery capacity of 0.4 GWh via Lithium-ion technology [20]. Load variations in the HB plant should be allowed to circumvent the need for enormous battery storage sizes. For example, the patent of Ostuni et al. [21] showed the capability to regulate the NH_3 synthesis system's load by controlling the reactor's inlet temperature, the inert gas concentration and the purge flow rate of the process. This control over the HB unit reduces the minimal load between 10% to 20% below the nominal load. The research of Cheema et al. [22] also demonstrated this capability of extending the flexibility for variable loads with adapted NH_3 reactor configurations. Cheema et al. [22, 23] concluded that changing the inert feed concentration, the feed flow rate and the H_2/N_2 ratio to the process creates the highest flexibility for the $PtNH_3$ process to operate when powered by intermittent power sources. Beerbühl et al. [24] developed a heuristic optimization approach to integrate renewable energies through the optimal sizing and scaling of the chemical processes. The study applied this approach to a non-linear NH_3 synthesis process and established the necessity of using non-linear modeling to optimize the scheduling and capacity planning of these H_2-based storage facilities. Other papers, such as the ones of Nayak-Luke et al. [17, 25] and Palys et al. [26] showed how this scheduling and advanced power management strategies achieve lower LCOA by minimizing the H_2 and N_2 buffer tank capacity. In particular, the study of Nayak-Luke et al. [17] presented cost-competitive

locations in 2030 by adopting this strategic scheduling in combination with a reduction in the levelized cost of electricity and capital expenses of the electrolyzer. The strategy involved perfect forecasting of solar and wind power over the year for each location and optimizing the allocation of this electric energy to the electrolyzer, HB and Air Separation Unit (ASU). This strategic scheduling aimed at minimizing the H_2 buffer storage during the year and maximizing the total NH_3 production to minimize the LCOA. The study included a 30 minute or hourly time resolution (depending on the location) for this analysis. The results showed that locations in Europe with high average wind power production could only reach an LCOA below 450 USD/tonne$_{NH_3}$ when the electrolyzer's full load hours (i.e. the ratio of energy consumed and the nominal power of the electrolyzer) are over 5000 h. Instead, in Northern Africa, the electrolyzer needs a full load hour between 2500 h and 3000 h to achieve a similar LCOA [17]. This reduced load hour is achieved by the reduced levelized cost of electricity (with solar power) for regions with higher solar irradiance [27]. However, these studies do not consider uncertainties related to changes in cost and energy consumption while optimizing the design of such energy capture systems. These cost variations already influenced the traditional NH_3 production process, where natural gas is transformed via the steam methane reforming process to produce H_2. To the recent price increase of natural gas in Europe, the largest fertilizer plant in Belgium had to temporarily shut down its NH_3 and ammonium production [28]. Recently, another NH_3 producer decided to terminate its operation in Germany to these high gas prices [29]. We can avoid this issue with the renewable-powered $PtNH_3$ plant by considering price variations as economic uncertainty and including technical uncertainties in the design phase. We can then measure the collective impact of these uncertainties on the performance indicators, i.e. price of NH_3, efficiency, operational flexibility or carbon footprint.

As uncertainties on the techno-economic $PtNH_3$ system parameters will affect the chosen performance indicators, we have to quantify the total impact of uncertainties on a performance indicator concerning probabilistic input parameters, where Uncertainty Quantification (UQ) can be adopted. In this frame-

work, crude Monte Carlo Simulation is a state-of-the-art method that quantifies the statistical moments on the performance indicator based on a large set ($10^4 - 10^5$) of randomly generated scenarios from the distributions on the input parameters [30]. As a large set of model evaluations is required, the method is computationally intractable when the model takes more than a few minutes to calculate the result for a single scenario [31]. Therefore, to ensure computational tractability on heavy models, surrogate-assisted UQ constructs a surrogate model of the system model for the space defined by the probabilistic input parameters (i.e. the stochastic dimension) [32]. Typical surrogate modelling techniques include Kriging [33], support vector machines [34], ANalysis Of VAriance (ANOVA) [35] and Polynomial Chaos Expansion (PCE) [36]. In the case of PCE, the statistical moments (e.g. mean, standard deviation) and the global sensitivity indices (i.e. Sobol' indices) can be quantified analytically from the coefficients. In assessing the importance of electrofuels in the Belgian energy mix, Rixhon et al. [37] used PCE to perform UQ on the total cost of the future Belgian energy system. They highlighted the importance (53%) of the uncertainty related to the cost of importing electrofuels.

When uncertainties are considered during model evaluation—and the performance indicators are uncertain—an optimization under uncertainty should be adopted to optimize the system. For renewable energy systems, stochastic programming and robust optimization are the most common approaches [38]. Stochastic programming is a scenario-based approach where the expected performance is optimized, considering probabilistic input uncertainties [39]. Zakaria et al. [40] provided a comprehensive overview of stochastic programming applications on renewable energy systems. Alternatively, robust optimization in a Mixed Integer Linear Programming (MILP) framework optimizes the design under the worst-case combination of the input parameter values [41]. However, this method's nested anti-optimization routine to find the worst-case scenario can become computationally intractable for a high stochastic dimension. Besides, over-conservative designs are generally proposed, as the worst-case design might correspond to a scenario with nearly zero probability of occurrence [42].

An alternative robust optimization approach—known as Robust Design Optimization (RDO)—optimizes the expected performance (i.e. the mean) and minimizes the variability in that performance (i.e. the standard deviation) while including all implemented uncertainties simultaneously [43]. Thus, RDO provides robust designs that are least sensitive to the random environment, defined by the input uncertainties. Therefore, robust designs are needed to reduce the sensitivity of these technical and economic uncertainties and quantify the effect of these uncertainties on (technical or economic) objectives [44].

RDO is commonly adopted in ship design [45], structural mechanics [46] and aerospace engineering [47]. However, RDO applications on renewable energy systems remain limited [48]. Recently, Verleysen et al. applied RDO on the NH_3 production of a wind-powered PtNH_3 system with a steady-state model in Aspen Plus [49] and on a dynamic model in Python [50]. Coppitters et al. [51] optimized the design of a photovoltaic array with battery and H_2 storage for the Levelized Cost Of Electricity (LCOE), illustrating that energy storage reduced the uncertainty on the LCOE by 42%.

Within this study, we disregard the reconversion of NH_3 back to H_2 or electricity and assume that NH_3 will be used in the fertilizer or power industries. This NH_3-to-power conversion and its levelized cost of electricity are studied by Cesaro et al. [52], where three different types of NH_3-fueled combined cycle gas turbines are assumed. The study concluded that the LCOE of NH_3-to-power systems would range between 167 USD_{2021}/MWh and 197 USD_{2021}/MWh by 2040, depending on the fraction of NH_3 converted to H_2, making it compatible with the combined cycle gas turbines (between 0% and 100%) assuming an NH_3 price of 380 $\mathrm{USD}_{2021}/\mathrm{tonne}_{\mathrm{NH_3}}$ and a plant's capacity factor of 25%. Cesaro et al. showed with a sensitivity analysis that the NH_3 price significantly influences the LCOE of the NH_3-to-power conversion [52].

In this paper, we performed a robust design optimization on a PhotoVoltaic (PV) powered grid-connected PtNH_3 plant in Belgium and an isolated PV-powered PtNH_3 plant in Morocco, where NH_3 is transported through shipping to Belgium. The novelty of this paper lies within the adoption of combining

economic and technical uncertainties for a power-to-NH_3 plant and optimizing the design of these plants with an RDO methodology. This study aims to find the optimal energy efficiency and lowest LCOA while minimizing their sensitivity to uncertainties. The optimizer determines the size of all individual components (PV array capacity, the electrolyzer capacity, the backup system, the buffer tanks, and HB capacity) and power flows to maximize the mean $PtNH_3$ energy efficiency, minimize the mean LCOA and the standard deviation of each of these Quantities of Interest (QoI). With a sensitivity analysis, we can determine the uncertainties that significantly impact these QoI and provide further recommendations to reduce the sensitivity of each objective.

2. Methodology of the power-to-ammonia plant

This section first introduces the global $PtNH_3$ model, describing how each component is modeled (Subsection 2.1). Next, the climate data (Subsection 2.2) and the objectives (Subsection 2.3) are defined. Finally, we describe the RDO method (Subsection 2.4), combining a meta-heuristic optimizer and a UQ method, the design variables and uncertainties affecting the cost and system performance are described.

2.1. Solar-powered ammonia synthesis process

The solar-powered $PtNH_3$ model can be divided into five main parts (Figure 1). The first part converts solar irradiance to electric energy using PV cells. The second part transforms the electric energy to H_2 and N_2, using a Proton Exchange Membrane (PEM) electrolyzer and an ASU. When the PV power to the electrolyzer exceeds its capacity, the electrolyzer operates at its maximum capacity and the excess power is provided to the ASU. When this power again exceeds the capacity of the ASU, the ASU operates at maximum capacity and discards any residual power. The third section stores the H_2 and N_2 gas in buffer tanks, resulting in a backup power system. A fuel cell stack or grid connection (or both) powers the NH_3 process when insufficient power is available

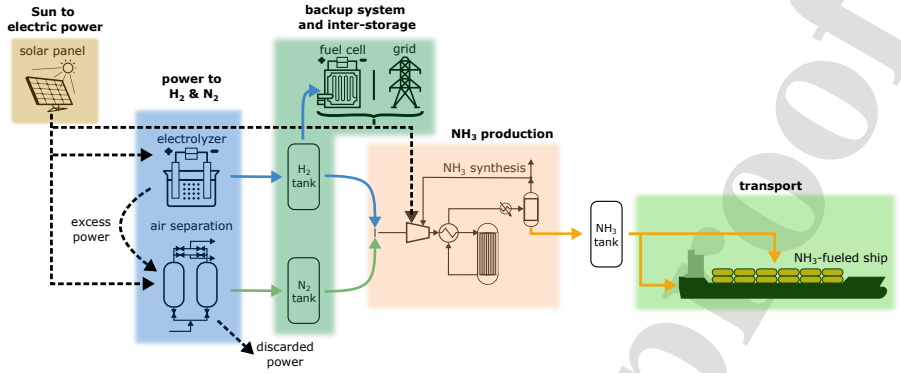

Figure 1: The flow chart of the Power-to-NH_3 plant where the plant is subdivided into five groups. The photovoltaic cell converts solar irradiance into electric power. This power is distributed over the production of H_2, N_2 and NH_3. The intermediate storage buffers the H_2 and N_2 gas, and a backup system provides power to the HB when there is insufficient solar power. In the case of the Moroccan PtNH_3 plant, a ship transports (and partially use) the NH_3 to Belgium.

to compensate for a set load. We did not include batteries as their capacity is limited [53], whereas a H_2 source is available for the fuel cell to produce electric power. In the fourth section, H_2 and N_2 are extracted from the tanks and provided to the HB to produce NH_3. The HB is powered directly by the PV panels or the backup system (grid and/or fuel cells). In the last section, the produced NH_3 is shipped from the Moroccan PtNH_3 plant to Belgium. The entire solar-powered PtNH_3 plant and ship model are developed in Python, as described in the following subsections.

2.1.1. Photovoltaic cells

To determine the electricity a PV array produces, we imported the model from the *PVlib* Python library [54]. This library adopted the models of De Soto et al. [55], which provided the five electrical parameters to determine the current-voltage curve at a certain irradiance and temperature for four PV cell types (monocrystalline, polycrystalline, silicon thin film, triple junction cell) modules. These electrical parameters were analyzed at standard rating conditions (irradiance of 1000 W/m^2 and cell temperature of 25°C). In addition, the model

considers the absorbed radiation, incidence angle modifier and air mass modifier (the distance the light travels through the atmosphere) to consider the slope and location of the installed PV module and the time of the year [55]. However, this model does not consider the efficiency deterioration of the PV panels over time by dirt and humidity [56, 57]. The model quantifies the PV panel power production through a current-voltage characteristic:

$$I_{\mathrm{PV}} = I_{\mathrm{L}} - I_0 \left(\exp\left(\frac{U + I R_{\mathrm{s}}}{n_{\mathrm{diode}} N_{\mathrm{s}} U_{\mathrm{th}}} \right) - 1 \right) - \frac{U + I R_{\mathrm{s}}}{R_{\mathrm{sh}}} \quad [\mathrm{A}], \tag{1}$$

for which the parameters are derived from manufacturer data [36]. We adopted the characteristics of a typical panel, the monocrystalline silicon PV panel (Sunpower SPR X-19-240-BLK) [58], as a reference for the operation of the PV array.

2.1.2. Proton exchange membrane electrolyzer and hydrogen tank

We adopted a PEM electrolyzer, which promises a fast response time (<1 second) and full operational flexibility. These characteristics are crucial when coupled with an intermittent renewable energy supply [59]. The H_2 production of a PEM electrolyzer is directly related to the operating current:

$$\dot{n}_{\mathrm{H_2}} = \frac{I_{\mathrm{PEM}}}{2F} \quad [\mathrm{mol/s}], \tag{2}$$

where I_{PEM} is the current in A and F is Faraday constant (96 485 s/(A mol)). To derive the operating current from the applied electric power, we adopted the voltage-current characteristic from Abdin et al. [60]. The operating current considers the open-circuit voltage U_{oc}, activation overpotential U_{act}, ohmic overpotential U_{ohm} and concentration overpotential U_{con}, which depend, among others, on the operating temperature, pressure and current:

$$U_{\mathrm{PEM}} = U_{\mathrm{oc}} - U_{\mathrm{act}} - U_{\mathrm{ohm}} - U_{\mathrm{con}} \quad [\mathrm{V}], \tag{3}$$

We refer to Abdin et al. [60] for the details on the quantification of these overpotentials.

The produced H_2 is then stored in a H_2 tank, where we define the energy stored in this tank by the Lower Heating Value (LHV) of H_2 (120 MJ/kg) and

the mass of H_2 in the tank in kg.

$$E_{H_2} = \mathrm{LHV}_{H_2} m_{H_2} \quad [\mathrm{MJ}] \tag{4}$$

A minimum capacity of 10% is assumed to allow a maximum depth of discharge of 90% as described by Wang et al. [61]. We did not consider the intermediate compression of H_2 as it would require additional steps in power management and assumed no pressure and mass losses inside the tank. These mass losses occur during production and long-term H_2 storage (above one month) where Genovese et al. [62] showed that these losses mainly occur during pipe leakages, malfunctioning valves and maintenance activity. The study reported monthly H_2 losses between 2% and 37%, which mainly depended on the system maintenance, operation and storage level of the piping, buffer tank and compressors during each month. We need to minimize its capacity to reduce the cost related to this H_2 tank, as presented by Nayak-Luke and Bañares-Alcántara [17].

2.1.3. Air separation unit and nitrogen tank

The ASU generates N_2 gas obtained from the air. The energy efficiency of the ASU varies depending on the adopted process (membrane, pressure swing adsorption or distillation), where the range of an ASU energy consumption ranges between 0.108 $\mathrm{kWh/kg_{N_2}}$ and 0.119 $\mathrm{kWh/kg_{N_2}}$ [17, 25, 63]. We included the three technologies in the system design procedure as the ideal size of this solar-powered NH_3 plant is investigated. To avoid modeling the intrinsic characteristics of the three processes, we implemented a linear relationship between the N_2 gas production (in kg/h) and the hourly electric energy consumed by the ASU with an uncertain energy efficiency between the identified range.

The produced N_2 is then assumed to be stored in an N_2 tank. Like in the case of the H_2 tank, the optimizer needs to minimize the maximum capacity of the N_2 tank (in kg) as presented by Nayak-Luke and Bañares-Alcántara [17]. We assume the same maximum depth of discharge of the H_2 tank and no pressure and mass losses inside the tank. We integrated a capital expense of 19.0 $\mathrm{euro/kg_{N_2}}$ related to the size of the N_2 tank as indicated by Palys et al. [64].

2.1.4. Haber-Bosch synthesis process

The Haber-Bosch Synthesis (HBS) process synthesizes the H_2 and N_2 gas with a catalyst to NH_3. The efficiency of this synthesis loop depends on various operating conditions and design parameters, e.g. the loop pressure (ranges between 150 bar and 250 bar), the temperature inside the NH_3 reactor (reaching between 350°C and 550°C), the catalyst material, the type of separation process (via a condensation or pressure swing adsorption system) and the reactor configuration (direct or indirect cooling). This combination of elements and the capacity of the NH_3 synthesis system results in different energy consumptions for the HB process (between 0.532 kWh/kg_{NH_3} and 0.852 kWh/kg_{NH_3}) [17, 18, 25, 65]. We integrated a linear relation between the NH_3 production (in kg/h) and energy efficiency to avoid the development of a high-fidelity, non-linear model, creating a computational burden during the design optimization. To compensate for the linearization of the HB model, we implemented an uncertainty on this energy consumption (E_{HBS}). We assumed in this linear model that the process will constantly operate at a H_2/N_2 ratio of 3:1. In this regard, for each 17 kg of produced NH_3, 14 kg of N_2 and 3 kg of H_2 gas are removed from their respective buffer tanks. In addition, the load can only increase with steps of 20%/h between a designed minimum load and full load [64]. If the electric power to the HB increases and is larger than 20% of the previous load, the load will increase by 20%. The power diverges to the electrolyzer whenever this load is lower than 20%. When the power from the solar park decreases and is lower than 20%, the load will decrease by 20%. The backup system compensates for any difference between the energy consumption of the HB and the electric power. In addition, when the H_2 tank operates at its minimum (maximum) capacity to the seasonal availability of solar irradiance, the NH_3 production will decrease (increase). So, the NH_3 production will change to allow the H_2 buffer tank to recover from its boundary levels. For example, when the buffer tank reaches its maximum capacity, a higher NH_3 production during the night can occur, or when the buffer tank reaches its minimum capacity, the NH_3 produc-

tion will be minimized during the day. This load scheduling shows an improved overall efficiency and levelized cost to the decreasing dependency of grid or large backup systems in combination with the high H_2 storage cost [25, 64].

2.1.5. Backup system

We incorporated a backup system to accommodate a steady power supply to the ramp-limited HB process. So when there is insufficient electric power, e.g. a sudden decrease in solar irradiance or powering the plant at night, this backup system provides enough power to the HB to continue the NH_3 production. This backup system could be provided via a dispatchable grid or a fuel cell stack. For the case of Belgium, we assume that a power grid is always available, like in the case of Armijo and Philibert [18]. To reduce this grid dependency, a fuel cell stack can be deployed like in the study of Palys et al. [64]. For Morocco, we assume this plant will be grid-isolated and fully backed up by a fuel cell-based system like in Nayak-Luke et al. [25]. We chose this configuration (grid-connected Belgian case and grid-isolated Moroccan case) because of the countries' different technical and environmental situations. A high-voltage grid connection is already available in Zeebrugge [66] to transfer the off-shore wind energy and inject it into the electricity grid. For Morocco, this high-voltage grid connection is unavailable in Aglou [67]. In addition, the carbon intensity of the electricity production in Morocco in 2022 was $0.61\,kg_{CO_2}$/kWh, while the carbon intensity of Belgium in 2022 was $0.157\,kg_{CO_2}$/kWh [68]. As the carbon intensity of Morocco is 3.89 times higher than in Belgium, and the high-voltage connection is not available in Aglou, we did not consider a grid-connected $PtNH_3$ plant in Morocco. Liu et al. indicated that the grid's carbon footprint influences the $PtNH_3$ plant depending on how the grid is used, e.g. as a backup to ensure a constant NH_3 production or powering the electrolyzer [69]. The authors demonstrated that if H_2 is produced solely via the grid with a carbon footprint of $0.6\,kg_{CO_2}$/kWh, the carbon footprint of NH_3 would be $5.9\,kg_{CO_2}/kg_{NH_3}$, which is between 2 and 3 times larger than the traditional NH_3 plant [69]. In addition, when the grid is used as backup power to ensure a constant NH_3 production,

the carbon footprint would drop to $0.27\,\mathrm{kg_{CO_2}/kg_{NH_3}}$. When the grid's carbon footprint decreases to $0.3\,\mathrm{kg_{CO_2}/kWh}$, the carbon footprint of NH_3 would go to $0.13\,\mathrm{kg_{CO_2}/kg_{NH_3}}$ [69]. When considering the impact of the cost of a grid connection, Salmon et al. examined the influence of a grid-connected $PtNH_3$ plant which can only consume from the grid. They demonstrated that a reduction of LCOA is always achieved. However, this reduction depends on the location's renewable energy potential, the average levelized cost of electricity and if there is already a grid connection [70]. For our work, whenever there is no grid and the backup capacity is insufficient to support the HB process at a particular hour, the NH_3 production is set to zero for the residual year.

The PEM fuel cell is characterized similarly to the PEM electrolyzer. The voltage-current characteristic is adopted from Murugesan et al. [71], which has been validated on the Ballard-Mark-V PEM fuel cell:

$$U_{\mathrm{PEMFC}} = U_{\mathrm{Nernst}} - U_{\mathrm{act}} - U_{\mathrm{ohm}} - U_{\mathrm{con}} \quad [\mathrm{V}]. \tag{5}$$

We refer to the work of Murugesan et al. [71] for the detailed quantification of these overpotentials.

2.1.6. Ammonia-fueled ship model

A ship transports NH_3 from Morocco (Aglou) to Belgium (Zeebrugge), where we adopted a ship with an NH_3-based engine propulsion system. This propulsion system removes the need for heavy fuel oil as the current maritime fuel. Several projects have shown interest in decarbonizing the maritime sector by adopting NH_3 or H_2 as an alternative fuel [72, 73]. NH_3 is chosen in this study because of its lower onboard storage costs than H_2 [74], while the combustion of NH_3 provides for short-term reduction of greenhouse gasses and lower costs than fuel cells [75]. Therefore, we adopted the ship model with an NH_3-fueled internal combustion engine reported in Kim et al. to transport NH_3 across the two countries [74]. The reported ship has a maximal capacity of 500 refrigerated containers (reefers) with a volume of $28.3\,\mathrm{m^3}$. We assumed the transported NH_3 is stored as a liquid at a pressure of 11 bar and 27°C, having a density of

$600\,kg/m^3$ [76]. We integrated the same ship model (Case 2 in Kim et al. [74]) and its load profile while including the economical parameters of the ship's components. The study reported a daily fuel consumption of $69.9\,tonne_{NH_3}$ with 250 reefers, which could transport 4290 tonne NH_3 with each trip in our case. However, we adapted the electric service profile of the ship with a linear scaling factor. This scaling factor allows the optimizer to design the total reefer capacity of the ship, i.e. more reefers on the ship can transport more NH_3 but increase fuel consumption. When the number of reefers is relatively small, e.g. one reefer, less NH_3 is transported, and less fuel will be consumed (21.6% less fuel consumption between a capacity of 1 and 500 reefers). Based on the maximum speed of the ship (a maximum speed of 19 knots [74]), the ship will spend between 3 and 4 days traveling from Aglou to Zeebrugge [77]. We refer to the study of Kim et al. for more details on the ship's fuel consumption and the related cost of the propulsion system [74].

2.2. Climate data

As climate data, we adopted the hourly ground solar irradiance and ambient temperature in Belgium (Zeebrugge) and Morocco (Aglou) to the PV-powered $PtNH_3$ plant (Figure 2). This climate data is obtained via renewables.ninja [78]. We observe a significant difference (41.8%) in the yearly solar irradiance in the two locations. The location in Morocco (Aglou) shows a more stable solar irradiance over the year, whereas the solar irradiance in Belgium (Zeebrugge) is more affected by the weather and seasons.

2.3. Quantities of interest

This work aims to optimize the system according to two critical aspects during the design phase of a $PtNH_3$ plant, i.e. the energy efficiency and the levelized cost of NH_3. Optimizing the design to increase energy efficiency results in a lower energy consumption to produce the same amount of NH_3. Considering the levelized cost of the $PtNH_3$ system during the design optimization ensures that the design is economically viable and can compete with traditional NH_3

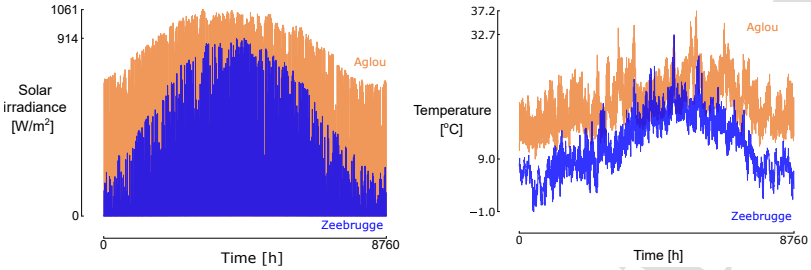

(a) Hourly ground-level solar irradiance data of Zeebrugge (Belgium) and Aglou (Morocco).

(b) Hourly air temperature data of Zeebrugge (Belgium) and Aglou (Morocco).

Figure 2: Climate data of Zeebrugge (Belgium) and Aglou (Morocco) [78].

production methods. Therefore, the techno-economic QoIs for the $PtNH_3$ system are the LCOA and the total energy efficiency of the $PtNH_3$ plants (η_e). The LCOA is defined as:

$$\text{LCOA} = \frac{\sum_i \left(\text{CAPEX}_{a,i} + \text{OPEX}_{a,i}\right) + C_{\text{grid}}}{m_{\text{NH}_3}} \quad [\text{euro/tonne}_{\text{NH}_3}], \tag{6}$$

where the LCOA depends on the total annualized investment cost ($\text{CAPEX}_{a,i}$) and annualized operational cost ($\text{OPEX}_{a,i}$) of each component i, the grid cost (C_{grid}) and the yearly NH_3 production (m_{NH_3}). We implemented the method of Zakeri and Syri [79] to convert the capital expense per installed capacity (CAPEX_i) of each component i to its annualized investment cost ($\text{CAPEX}_{a,i}$) by considering the Capital Recovery Factor (CRF) of each component:

$$\text{CAPEX}_{a,i} = CRF\ C_i\ \text{CAPEX}_i, \tag{7}$$

where C_i is the installed capacity of component i. The CRF factor is defined by the components lifetime n and the real discount rate r:

$$CRF = \frac{r(1+r)^n}{(1+r)^n - 1}, \tag{8}$$

where the real discount rate r is determined by the inflation rate f and the discount rate at the start of the loan r_{start}:

$$r = \frac{r_{\text{start}} - f}{1+f}. \tag{9}$$

We considered a lifetime of 30 years for each component of the $PtNH_3$ plant and ship [17, 18], used a starting discount rate of 4%, an inflation rate of 2% while adopting a grid price of 71.5 euro/MWh [51]. The following subsection provides further details on each component's CAPEX and OPEX. The technical quantity of interest is the energy efficiency of the plant. As the energy consumption of the HB and ASU are linearized, we can quantify the impact of this linearization on the energy efficiency as our QoI via the UQ analysis of certain designs. This linearization imposes an inaccuracy in the performance of these systems at partial loads, as is described by Schulte Beerbühl et al. [24]. By adopting an uncertainty on the energy consumption, we can measure the effect of this linearization on this QoI. We defined this energy efficiency as the ratio of the total NH_3 production (E_{NH_3}) and the total amount of energy (E_{total}) provided to the system.

$$\eta_e = \frac{E_{NH_3}}{E_{total}} \quad [-] \tag{10}$$

This total energy is composed of two parts: the energy provided to the system via the PV panels (E_{PV}) and the energy supplied by the grid (if the grid is available). To penalize the excessive storage or usage from the H_2 and N_2 buffer tanks, the energy in these tanks is subtracted from the produced NH_3. This penalization avoids the buildup or single use of H_2 and N_2 in the buffer tanks when the PV array is oversized or undersized, respectively. The energy efficiency of the $PtNH_3$ plant design is therefore defined as follows:

$$\eta_e = \frac{m_{NH_3} \cdot \mathrm{LHV}_{NH_3} - |E_{H_2,\mathrm{tank}}| - |E_{N_2,\mathrm{tank}}|}{E_{PV} + E_{grid}} \quad [-], \tag{11}$$

where m_{NH_3} amount of NH_3 produced over the year in kg, LHV_{NH_3} is the Lower Heating Value of NH_3 (18.6 MJ/kg_{NH_3}), E_{H_2} and E_{N_2} are the energy in the H_2 and N_2 tank at the end of the year, E_{PV} is the electric energy produced by the solar panels and E_{grid} is the consumed grid energy in MJ. We compute the N_2 energy based on the N_2 mass in the tank at the year's end and the ASU's specific energy consumption.

2.4. Robust design optimization

We use a UQ analysis to quantify the sensitivity of the objectives towards the d uncertain parameters. When obtaining the objectives' statistics (mean and standard deviation), we can use a meta-heuristic optimizer to find the set of optimized design variables of the $PtNH_3$ process concerning these statistical moments. These principles are implemented in the RDO Python framework Robust design optimization of renewable Hydrogen and dErIved energy cArrier systems (RHEIA) [80], where the genetic algorithm acts as the outer loop, providing sets of design samples $\boldsymbol{v}$ to the energy model (Figure 3). Then, an inner

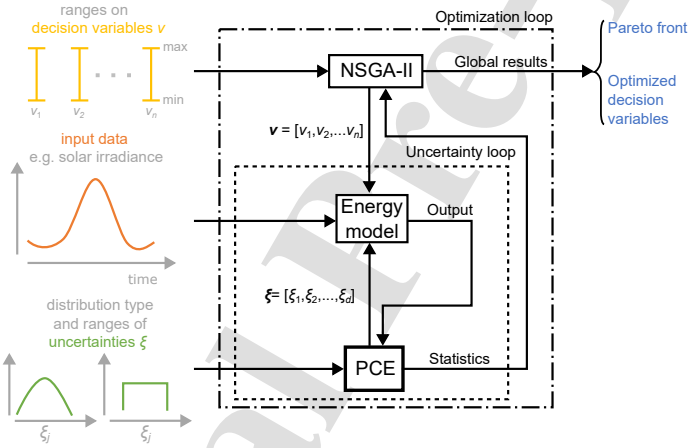

Figure 3: Robust design optimization algorithm where the genetic algorithm operates as the outer loop and the PCE in the inner loop. In the outer loop, the NSGA-II algorithm provides a set of design samples to the energy model (i.e. $PtNH_3$ model). Then, in the inner loop, the PCE algorithm computes the mean and standard deviation of each objective (i.e. LCOA and energy efficiency) for each design sample. These statistical moments (mean and standard deviation for LCOA and energy efficiency) are provided to the genetic algorithm as objectives.

loop is initiated where each design sample v_i undergoes an uncertainty quantification analysis. The analysis determines the mean and standard deviation on the QoI for that design sample by propagating the d uncertain parameters ξ. The mean and standard deviation for each QoI from each design sample set is then fed back to the genetic algorithm. The best-performing design samples

are stored, and new design samples are generated, for which the mean and standard deviation on the QoI is quantified again in the inner loop. This process is repeated until a stopping criterion is met, which evaluates these results and proceeds to generate new designs that need to be evaluated in the uncertainty loop. Further details on the applied genetic algorithm and uncertainty quantification method are described next.

2.4.1. Genetic algorithm: the RDO's outer loop

We implemented the multi-objective Nondominated Sorting Genetic Algorithm (NSGA-II) [81] to determine the model's optimized set of design variables. In the first generation, the algorithm produces an initial set (population) of design samples (N samples) through Latin Hypercube Sampling (LHS) [82]. These design samples are then evaluated through the energy model and assigned a fitness value (the objective function). From these values, the algorithm determines the best fitness values according to two performance indicators: the rank of each design and its crowding distance. The rank is assigned through the non-dominated sorting concept. This concept defines that design A dominates design B when no objective of design B is performing better than any objective in design A, and at least one objective of design B is performing better for the same objective of design A. Each non-dominated design is then assigned a rank, e.g. rank 1, which corresponds to the first non-dominated front. Then, these designs are removed from the original population, and the residual designs are ranked, i.e. rank 2, and removed from the population. This procedure is repeated until every design is assigned a rank. After the design ranking, the crowding distance assigns each design a measure of how close a fitness value is to the other fitness values. A larger crowding distance results in greater diversity in the population, which could aid in finding better fitness values [83]. After the non-dominating sorting and crowding distance operations, a second design sample set (second generation) of N samples is created via selection, crossover and mutation operators of the first generation. Selection is based on the rank and the crowding distance, where the design with the best rank and largest

crowding distance is selected over other designs. In the crossover step, designs are combined to form a new unique design. Lastly, mutation randomly changes a part of a design to increase the diversity within the population. After evaluating the second generation, the first and second generations of design samples are combined, creating a $2N$ sample set. The fitness values of this combined set are ranked again according to their non-dominance and crowding distance. The best N samples of one or multiple non-dominance levels and crowding distances are adopted in the next generation through the same selection, crossover and mutation procedures, creating the next generation of designs [84]. This iterative process is repeated until a predetermined number of generations is achieved (computational budget is exceeded), or the simulation converges towards a solution (stopping criterion). Depending on the relation between the multiple objectives, the optimized set of design samples can converge to a single optimized design sample (i.e. non-conflicting objectives) or a set of optimized design samples (i.e. conflicting objectives). In such a set of optimized design samples, each sample dominates every other sample in at least one objective, i.e. Pareto frontier.

2.4.2. Polynomial Chaos Expansion: the RDO's inner loop

The PCE algorithm is adopted to quantify the impact of the uncertainties on the QoI [85, 86]. This technique provides a computationally efficient alternative to the slow but always converging Monte Carlo simulation technique, which needs above 10^4 number of samples to converge to the mean and standard deviation, as was the case in the study of Laššák et al. [87] and Torre et al. [88]. This MCS method is intractable when we subjugate an expensive-to-evaluate model. To quantify the mean and standard deviation of the QoI efficiently and with fewer training samples, the PCE algorithm creates a surrogate model $\hat{M}(\boldsymbol{\xi})$ of the expensive-to-evaluate model $M(\boldsymbol{\xi})$ based on multivariate orthogonal polynomials Ψ_i and corresponding coefficients a_i:

$$M(\boldsymbol{\xi}) \approx \hat{M}(\boldsymbol{\xi}) = \sum_{i=0}^{P} a_i \Psi_i(\boldsymbol{\xi}). \tag{12}$$

When P in Equation 12 is infinite, the surrogate model is an exact representation of the physical model. In practice, the series is truncated depending on the complexity of the input-output relation (related to the polynomial order p of the polynomials Ψ_i), and the stochastic dimension d (corresponding to the number of imposed uncertainties) [89]. The number of terms P for constructing the truncated series is defined by:

$$P + 1 = \frac{(p+d)!}{p!d!}. \tag{13}$$

As the multivariate orthogonal polynomials $\Psi_i(\boldsymbol{\xi})$ can be determined and the response of the model $M(\boldsymbol{\xi})$ is known, the coefficients a_i can be calculated via regression of $2(P+1)$ training samples necessary to determine these coefficients. When the PCE surrogate model is constructed, the mean μ and the variance σ^2 are derived analytically from the coefficients:

$$\mu = a_0, \tag{14}$$

$$\sigma^2 = \sum_{i=1}^{P} a_i^2. \tag{15}$$

Next to the statistical moments of the QoI, the contribution of each input parameter to the objective variation can be quantified through Sobol' indices S. The first-order Sobol' indices (i.e. no input parameter interaction considered) are defined as:

$$S_i = \frac{D_i}{D} = \frac{\mathrm{Var}[M(\xi_i)]}{\mathrm{Var}[M(\boldsymbol{\xi})]}. \tag{16}$$

Similar to the mean and variance, these first-order Sobol' indices can be quantified analytically via the PCE coefficients:

$$S_i^{PCE} = \sum_{\alpha \in A_i} a_\alpha^2 / D \qquad A_i = \{\alpha \in A : \alpha_i > 0, \alpha_{j \neq i} = 0\}. \tag{17}$$

The total Sobol' indices $S_i^{T,PCE}$ can be computed to consider the interaction between other input parameters:

$$S_i^{T,PCE} = \sum_{\alpha \in A_i^T} a_\alpha^2 / D \qquad A_i^T = \{\alpha \in A : 0 < \alpha_i\}. \tag{18}$$

The Leave-One-Out (LOO) cross-validation estimate can determine the accuracy of the PCE surrogate model. This LOO error (ϵ_{LOO}) quantifies the effect of removing one sample (i) from the training set and creating a PCE surrogate model $\hat{M}^{/i}$ from the residual training samples. Then the difference between the outcome of the actual model M and the surrogate model $\hat{M}^{/i}$ is quantified. Ultimately, the LOO error represents the mean square error of these differences if each training sample is removed once [83]:

$$\epsilon_{LOO} = \frac{1}{n}\sum_{i=0}^{n}(M(\xi_i) - \hat{M}^{/i}(\xi_i))^2. \tag{19}$$

To the properties of the PCE, this LOO error can analytically be computed via one PCE surrogate model $\hat{M}(\cdot)$ as is presented by Blatman et al. [90]. Finally, to accurately determine the mean, standard deviation and Sobol' indices, the LOO error needs to be minimized. We can decrease the LOO error by increasing the polynomial order p. This process can be repeated but would increase the number of training samples from the expensive-to-evaluate model and could lead to overfitting, increasing the LOO error instead [31].

In conclusion, combining the NSGA-II and PCE provides a method to perform RDO on the $PtNH_3$ model. The PCE algorithm determines the sensitivity of a particular design according to the input uncertainties and provides the mean and standard deviation of each QoI to the NSGA-II. This NSGA-II ranks each design according to the mean and standard deviation of each QoI and generates new design samples based on the most optimal results. This RDO methodology provides designs with optimized mean and lowest standard deviation, i.e. robust, of each objective.

2.4.3. Design space and uncertainty characterization

The $PtNH_3$ system is sized according to a set of design variables to minimize the levelized cost and maximize the system's efficiency. We selected eleven design variables that influence these objectives (Table 1). From these eleven design variables, eight design variables are used for sizing an individual component, i.e. the PV array capacity, the PEM capacity and FC stack size, the HB process

capacity, the H_2 and N_2 tank capacity and the number of reefers. The capacity ranges of these design variables are based on the results of the metaheuristic optimization used in the study of Nayak-Luke et al. [17]. This study showed in a deterministic environment (i.e. no uncertainties) for Belgium and Morocco that the optimized capacity size of the electrolyzer ranges between 168 MW and 262 MW and the H_2 tank capacity ranges between 44 ton and 132 ton. The residual three design variables are dedicated to the power distribution between the PEM stack and the HB process and determining the optimal minimal load of the HB process.

Table 1: Ranges of the design variables to be optimized by the NSGA-II algorithm.

Design variable	Minimum	Maximum	Unit
PV capacity	1	10^6	[kW_p]
PEM capacity	1	10^6	[kW]
FC capacity	1	10^5	[kW]
HBS capacity	1	10^5	[kW]
ASU capacity	1	10^5	[kW]
H_2 tank	1	10^5	[kg]
N_2 tank	1	10^5	[kg]
reefer	1	500	[-]
fraction P_{PV} to P_{HBS}	1	20	[%]
fraction ($P_{PV} - P_{HBS}$) to P_{PEM}	80	99	[%]
HBS minimal capacity	10	50	[%]

For the uncertainty characterization, we identified seventeen uncertainties divided into twelve economic and five technical uncertainties. These economic uncertainties are extracted from the reported $PtNH_3$ studies, where these studies imposed deterministic values for the CAPEX and OPEX of the corresponding components. As these costs vary between these reports, we imposed the related CAPEX as uncertainties and converted the reported currencies to $euro_{2022}$. The range of each component is then determined and used as a uniform uncertainty

(Table 2). The uncertainty range of the OPEX of each component is considered between 1% and 3% of the corresponding components CAPEX.

Table 2: Economic uncertainty ranges of the capital and operational expenses of components of the $PtNH_3$ plant, where the reported currencies are converted into $euro_{2022}$.

Component	$CAPEX_i$			
	Minimum	Maximum	Unit	Source
PV	350	921	[euro/kW_p]	[17, 18, 26, 51]
PEM	482	1223	[euro/kW]	[8, 17, 18, 26, 91]
HBS	455	5317	[euro/kW]	[18, 26, 91]
ASU	1391	7162	[euro/(kg/h)]	[17, 18, 26, 92]
FC	921	2400	[euro/kW]	[17, 18, 26, 51]
H_2 tank	189	1420	[euro/kg]	[17, 18, 26, 93]

Table 3: Technical uncertainty ranges of the Power-to-NH_3 plant.

Component	Minimum	Maximum	Unit	Source
Specific energy consumption HBS	0.532	0.852	[kWh/kg]	[16–18, 25, 65]
Specific energy consumption ASU	0.108	0.119	[kWh/kg]	[17, 25, 63]
Hourly solar irradiance Belgium deviation	-4.19	4.19	[%]	[94]
Hourly solar irradiance Morocco deviation	-3.11	3.11	[%]	[94]
Hourly temperature Belgium deviation	-0.589	0.589	[°C]	[94]
Hourly temperature Morocco deviation	-0.145	0.145	[°C]	[94]
Shipping day (one trip)	3.0	4.0	[days]	[77]

For the first four technical uncertainties, we implemented the energy efficiency ranges of the HB process, the air separation, the solar irradiance and the ambient temperature of both locations (Table 3). We based the uncertainty of these locations' solar irradiance and ambient temperature on weather data for 11 years (between 2005 and 2016) [94]. In Aglou (Morocco), we observed a relative standard deviation on the yearly global irradiance and ambient temperature of 3.11% and 0.145°C, whereas, in Zeebrugge, these values correspond to 4.19% and 0.58°C. These uncertainties scale the hourly solar irradiance and

temperature of the climate data of Morocco and Belgium. The fifth technical uncertainty considers the time the ship travels from one port to another. According to a calculation tool [77], the ship takes between 3 and 4 days to reach the other port, which affects the ship's fuel consumption, whereas the ship is fueled by the NH_3 transported in the ship. We consider these uncertain technical parameters as uniform distributions (as we do not hold information on the distribution) except for the solar irradiance and temperature; we consider them Gaussian distributions as these uncertainties possess natural randomness [49, 86, 95].

3. Results and discussion

In this section, we first present the design optimization results (with and without uncertainties) and compare the deterministic and robust design cases (Subsection 3.1). Afterward, we discuss and compare the key design variables of the Moroccan and Belgian PtNH_3 processes (Subsection 3.2). Finally, we present the sensitivity indices of the uncertainties and discuss their influence on the results (Subsection 3.3).

3.1. Deterministic versus robust design optimization

For the NSGA-II algorithm, we choose a population N of 30 for each generation and a computational budget of 500 generations. The Deterministic Design Optimization (DDO) resulted in both cases in a Pareto front (Figure 4a). The Belgian case attains higher energy efficiencies (55.1%) than the Moroccan case (51.7%) at slightly higher cost (2305 euro/tonne_{NH_3} compared to 2238 euro/tonne_{NH_3} for Morocco). The efficiency difference between these two points is related to the backup system (fuel cell stack) and transport of NH_3, where each system uses H_2 or NH_3 as a fuel to power the plant via a fuel cell during the night or the ship during transport. The backup system and the ship account, respectively, for a 0.3% and 2.5% reduction in energy efficiency for the Morrocan case. When comparing the levelized cost of NH_3, the

Moroccan plant achieves a design with the lowest LCOA at a higher efficiency (540 euro/tonne$_{NH_3}$ and 45.7%) than the Belgian plant (757 euro/tonne$_{NH_3}$ at 50.9%). This Belgian LCOA is comparable to the ones found in the paper of Nayak-Luke et al. [17]. Nayak-Luke et al. observed that the LCOA of Belgium ranges between 731 euro$_{2022}$/tonne$_{NH_3}$ and 1258 euro$_{2022}$/tonne$_{NH_3}$ (between 737 USD$_{2020}$/tonne$_{NH_3}$ and 1269 USD$_{2020}$/tonne$_{NH_3}$). For the LCOA of Morocco, Nayak-Luke et al. found an optimal cost of 751 euro$_{2022}$/tonne$_{NH_3}$ (757 USD$_{2020}$/tonne$_{NH_3}$). For this case, our study considers different technical and economic parameters, whereas the study of Nayak-Luke et al. included wind power and location-dependent discount rates while excluding the shipping cost to deliver NH_3 to Belgium. However, the ship's cost (1% of the component cost) and fuel consumption (6.55% of the produced NH_3) are marginal. In comparison, we adopted for the deterministic optimization of both cases the average economic and technical parameters from other studies [8, 18, 26, 51, 91, 92] related to the cost of PV, PEM, ASU, HB and H_2 buffer tank, where these values differ from the ones reported in Nayak-Luke et al. [17]. Therefore, to include the uncertainties related to these parameters, the robust design optimization of the $PtNH_3$ of both locations must incorporate the range of possible values of

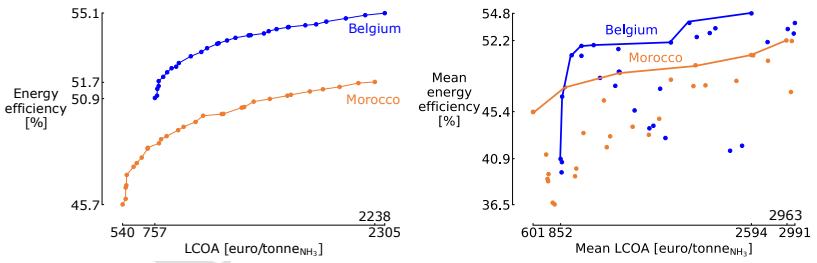

(a) Results of deterministic design optimization

(b) Results of robust design optimization

Figure 4: Deterministic and robust design optimization of PV-$PtNH_3$ plant of the Belgian and Moroccan case where maximizing the energy efficiency and minimizing levelized cost of NH_3 results in a trade-off.

these technical and economic parameters.

We selected the same NSGA-II parameters as the DDO for the RDO and chose a polynomial order p of 3 for the PCE algorithm. This polynomial order allowed a LOO error on the surrogate models of 2.97% on average. The RDO shows a similar Pareto front between maximizing the mean efficiency and minimizing the mean levelized cost of NH_3 (Figure 4b). Compared to the DDO, the uncertainties affect the LCOA and the energy efficiency in both cases. Similar to the DDO results, the Belgian RDO case attains a higher mean energy efficiency (54.8%) than the Moroccan case (52.2%) at a lower mean LCOA (2594 euro/tonne$_{NH_3}$ versus 2963 euro/tonne$_{NH_3}$). Still, the Moroccan plant achieves a lower LCOA at a higher efficiency (601 euro/tonne$_{NH_3}$ and 45.4%) than the Belgian plant (852 euro/tonne$_{NH_3}$ at 40.9%). Other trade-offs exist between optimizing the mean and minimizing the standard deviation of each objective (Figure 5). These results show the standard deviation of the LCOA and energy efficiency of both cases can be reduced by adapting the design. Also, the Moroccan plant shows a small trade-off in LCOA between the lowest mean

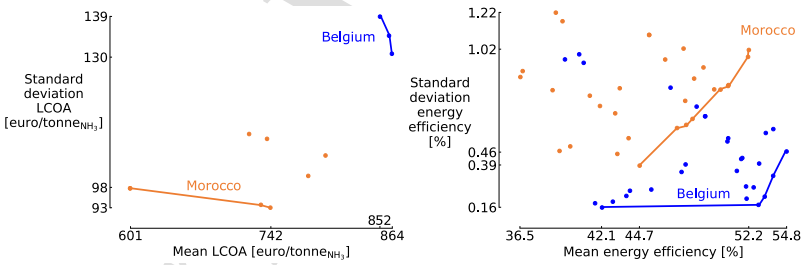

(a) Trade-off between mean and standard deviation LCOA

(b) Trade-off between mean and standard deviation energy efficiency

Figure 5: Pareto fronts of the mean and standard deviation of the LCOA and energy efficiency for the Belgian and Moroccan cases. The design trade-off between LCOA's mean and standard deviation of Morocco outperforms the designs on the Pareto front for the Belgian scenario. However, the optimized designs for the Belgian scenario outperform those for the Moroccan scenario in terms of expected efficiency (i.e. the mean) and robustness (i.e. the standard deviation).

and lowest standard deviation (Figure 5a). Between these extremes, there is a difference of 4.65 euro/tonne$_{NH_3}$ in standard deviation and 140 euro/tonne$_{NH_3}$ in mean. For the Belgian case, a similar design trade-off was observed where a difference of 8.92 euro/tonne$_{NH_3}$ in standard deviation and 12.0 euro/tonne$_{NH_3}$ in mean. In terms of energy efficiency, a small trade-off exists between the highest mean efficiency and the most robust design in the case of Belgium (12.7% difference in mean efficiency and 0.31% in standard deviation). The trade-off for the Moroccan case is similar to the Belgian case, where a difference of 7.50% is observed in mean energy efficiency and 0.63% in standard deviation (Figure 5b). In summary, the Belgian plant can reach higher mean and lower standard deviations in energy efficiency than the Moroccan plants. A part of the Moroccan's NH_3 production has to be consumed by the ship to transport the remaining NH_3 from Morocco to Belgium, thus resulting in lower mean energy efficiencies. In contrast, the Morrocan plants can achieve lower mean and standard deviations in LCOA than the Belgian plants with the lowest mean and standard deviation.

3.2. Key design variables

The Pareto fronts are defined by two key design variables: the capacity of the PV array and the PEM electrolyzer stack. This influence is best observed by the ratio of the PV over the PEM for each design (Figure 6). For the lowest mean LCOA of both cases, we observe that a PtNH_3 plant with a larger PV capacity than the PEM electrolyzer stack results in smaller levelized costs. The optimizer selects smaller electrolyzer capacities to reduce the plant's levelized cost as the PEM has a higher capital cost per power unit than the PV (852.5 euro/kW versus 635.5 euro/kW$_p$) on average. For the Morrocan case, the PV array capacity is 6% larger than the PEM electrolyzer capacity, while for the Belgian case, this is 139% (Figure 6a). This scale discrepancy is due to the climate difference; Belgium has a lower yearly solar irradiance (1101 kWh/m^2/year) compared to Morocco (2304 kWh/m^2/year), and the electricity production is also more affected by seasons than in Morocco. In both cases, the LCOA increases when the PV capacity decreases compared to the PEM capacity. However, this decrease

improves the mean energy efficiency (Figure 6b). As the PV and PEM capacities ratio decreases, more electric solar power is available to power the electrolyzer, decreasing the power input per electrolytic cell. This power decrease causes an increase in the electrolyzer cell efficiency as the overpotential losses are reduced due to lower current densities (Equation 3). In addition, we observe the same influence on the fuel cell capacity in the Moroccan case. To attain higher efficiencies, the fuel cell capacity increases from 1.56 times the capacity of the HB process (for the lowest LCOA mean) to 8.12 times (for the highest mean energy efficiency). Like with the electrolyzer, the fuel cell system is more efficient when the system becomes oversized, which increases the capital expenses but increases the energy efficiency of the $PtNH_3$ plant. In the case of Belgium, the fuel cell capacity is negligibly small, where all designs are fully grid-dependent. In addition, we observe that a minimal load between 10.0% and 12.3% of the NH_3 process is necessary to attain an efficient and low-cost design. Therefore, this optimization shows that an HB process that produces NH_3 at lower operating loads is necessary to create an energy-efficient and cost-effective $PtNH_3$ plant. So, further developing a flexible HB is vital for the future application of these seasonal energy capture systems.

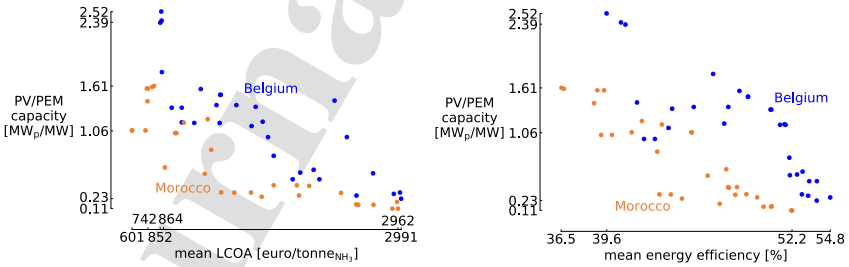

(a) The PEM/PV capacity ratio influence on the mean LCOA

(b) The PEM/PV capacity ratio influence on the mean efficiency

Figure 6: The ratio of the PEM and PV capacities influences the mean LCOA and efficiency of the Belgian and Moroccan cases.

3.3. Sensitivity indices

The sensitivity indices show for the analyzed designs the impact of each uncertain input parameter on the LCOA or energy efficiency. After analyzing the impact of all uncertainties, we present and discuss the three uncertainties with the most significant impact on each design and each objective.

In the UQ analysis of the designs with the lowest mean and lowest standard deviation in LCOA, we observe that these designs are all sensitive to the CAPEX uncertainties of the PEM electrolyzer ($CAPEX_{PEM}$) and the PV array ($CAPEX_{PV}$) (Figure 7a). In the Belgian case, the PV and PEM CAPEX uncertainties impact the standard deviation by 54.0% and 15.1% for the lowest mean LCOA design and 59.0% and 15.9% for the most robust design. For the Moroccan case, the lowest mean LCOA design is affected by the CAPEX uncertainty of PV and PEM electrolyzer by 31.2% and 42.3%, respectively. For the Morrocan plant with the robust LCOA design, the PV and the PEM CAPEX uncertainties dominate the standard deviation by 46.5% and 28.2%. The previous section shows that the impact difference originates from both cases' PV and PEM capacity. The PV capacity of the Belgian case with the lowest mean LCOA is 2.25 times larger than the lowest mean LCOA Moroccan case. So the PV CAPEX uncertainty has a more significant impact on the standard devia-

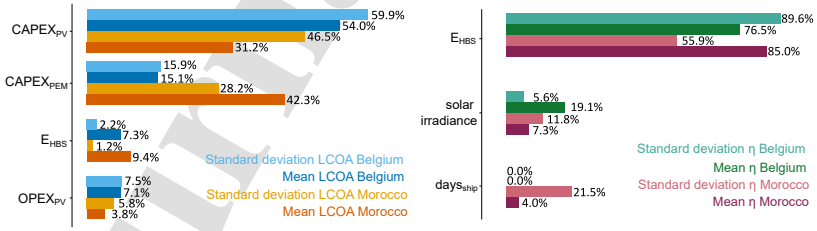

(a) Sobol' indices of the designs with lowest LCOA in mean and standard deviation.

(b) Sobol' indices of the designs with highest energy efficiency in mean and lowest standard deviation.

Figure 7: The UQ analysis shows that six out of nineteen uncertainties dominate the LCOA or energy efficiency of the $PtNH_3$ plant in Morocco and Belgium.

tion. If we look at the third largest Sobol' indices for the LCOA-related cases, we observe a difference between each objective and each case. In the robust Belgian and Moroccan case, the OPEX uncertainty of the PV ($OPEX_{PV}$) has the third largest effect (7.5% and 5.8%) on the standard deviation. This cost factor directly affects the levelized cost, as the PV CAPEX uncertainty also significantly affects this specific design. For the designs with the lowest mean LCOA in Belgium and Morocco, the UQ analysis exposes the impact of technical uncertainty on the levelized cost, i.e., the specific energy consumption of the HB (E_{HBS}). The specific energy consumption of the HB impacts the standard deviation of the design with the lowest mean LCOA in Belgium by 7.3% and 9.4% in Morocco. This uncertainty influences this design because it directly affects the NH_3 production during the year. In terms of the sensitivity to the energy efficiency, we observe that for the Belgian and Moroccan cases in both objectives (maximizing the energy efficiency and minimizing its standard deviation) dominate the results (Figure 7b). For Belgium, the uncertainty on the HB energy consumption dominates the results by 76.5% for the design with the highest mean and 89.6% for the design with the lowest standard deviation. The second most significant dominant factor is the yearly solar irradiance in the designs with the highest mean (19.1%) and lowest standard deviation (5.6%). These uncertainties directly impact the energy efficiency via the produced NH_3 and the available solar irradiance. For the Morrocan case, the HB process also dominates the energy efficiency in mean and standard deviation, respectively, by 85.0% and 55.9%. The second and third largest uncertainties in the energy efficiencies are the number of days the ship travels ($days_{ship}$) and the solar irradiance.

Overall, only six (three economic and three technical) out of nineteen implemented uncertainties are significant, where we showed only the three largest contributors to each design and each objective. The three economic uncertainties can be reduced by assuring the capital and operational expenses of the PV and PEM electrolyzer. Two of the three technical uncertainties can not be minimized as the uncertainty related to the solar irradiance is location-dependent,

while the travel days depend on the ship's route. However, the uncertainty related to the specific energy consumption of the HB can be reduced entirely by adopting a model representing the actual non-linear behavior of the NH_3 synthesis process. When we adopt this non-linear HB model, we could reduce the uncertainty related to the levelized cost and the standard deviation associated with energy efficiency. Examples of these high-fidelity models can be found in the study of Frattini et al. [96] and Araujo et al. [97].

4. Conclusion

In this study, we modeled all the components to transform solar energy into NH_3 and optimized this plant's energy efficiency and levelized cost with robust design optimization against technical and economic uncertainties. These uncertainties impact the $PtNH_3$ process for capturing and storing seasonal renewable energy. The results of this RDO showed that the Moroccan case provides designs with the lowest mean levelized cost (between 601 euro/tonne$_{NH_3}$ and 742 euro/tonne$_{NH_3}$) and least sensitive designs (between 98 euro/tonne$_{NH_3}$ and 93 euro/tonne$_{NH_3}$ in standard deviation). In the case of Belgium, a design trade-off for the LCOA was found between a design with a mean of 852 euro/tonne$_{NH_3}$ and a standard deviation of 139 euro/tonne$_{NH_3}$ and a design with a mean of 864 euro/tonne$_{NH_3}$ and a standard deviation of 130 euro/tonne$_{NH_3}$. In terms of energy efficiency, the Belgian case provided us with a design with the highest mean efficiency (54.8%) and a design with the lowest sensitivity (0.16%) on the standard deviation than in the Moroccan case (highest mean of 52.2% and lowest standard deviation of 0.39%) to the absence of an NH_3-fueled ship and fuel cell backup system. Overall, the Moroccan case results show that NH_3 plants in solar-rich conditions are cheaper and more robust (in terms of mean and standard deviation) to produce NH_3 remotely compared to local production. The trade-off between levelized cost and energy efficiency originates from two design variables: the PV and the PEM electrolyzer capacity. The Morrocan case attains lower PV capacities (compared to PEM capacity) while obtaining lower

levelized costs than the Belgian case. Decreasing this PV/PEM ratio increases the mean efficiency of the $PtNH_3$ plant for both cases. An additional design variable showed that for both locations, the HB plant needs a minimum load between 10% and 12.3%. Therefore, a flexible HB process is required to create an energy-efficient and cost-effective $PtNH_3$ plant. Regarding the sensitivity analysis, we observed that the standard deviations of the LCOA for the cheapest and most robust plant designs (in both locations) are mainly influenced by the capital cost uncertainties related to the PV array and PEM electrolyzer stack. In addition, the design with the lowest mean LCOA in Morocco and Belgium is also influenced by the uncertainty related to the energy consumption of the HBS process. Regarding the sensitivity of the energy efficiency in the Belgian and Morrocan plants, the uncertainty of the energy consumption of the HB and the solar irradiance have the most significant impact on the mean and standard deviations. In conclusion, the specific energy consumption directly influences the plant's energy efficiency and levelized cost (after the uncertainty of PEM and PV costs). In the current case, the uncertainty of the solar irradiance can not be further reduced as this is location-dependent. However, the location of the $PtNH_3$ plant can be optimized by using a Geographical Information System (GIS) as the one proposed by Huld et al. [94]. This PVGIS application can find the optimal location of a PV farm in Europe and Africa. Finally, the HB energy consumption uncertainty can be reduced by creating a model representing the HB process's non-linear behavior. Future work aims to perform a techno-economic-environmental evaluation of this robust design optimization, including environmental indicators like recycling of composite materials and depletion of rare materials.

5. Acknowledgments

D.C. acknowledges the support from the Belgian federal Energy Transition Fund, project DRIVER.

References

[1] IEA (2019), The Future of Hydrogen, Paris,, 2019. doi:10.1787/1e0514c4-en.

[2] C. Hank, A. Sternberg, N. Köppel, M. Holst, T. Smolinka, A. Schaadt, C. Hebling, H.-M. Henning, Energy efficiency and economic assessment of imported energy carriers based on renewable electricity, Sustainable Energy & Fuels 4 (5) (2020) 2256–2273. doi:10.1039/d0se00067a.

[3] P. Caumon, M. Lopez-Botet Zulueta, J. Louyrette, S. Albou, C. Bourasseau, C. Mansilla, Flexible hydrogen production implementation in the French power system: Expected impacts at the French and European levels, Energy 81 (2015) 556–562. doi:10.1016/J.ENERGY.2014.12.073.

[4] J. Fuhrmann, M. Hülsebrock, U. Krewer, Energy Storage Based on Electrochemical Conversion of Ammonia, in: Transition to Renewable Energy Systems, Wiley-VCH Verlag GmbH & Co. KGaA, Weinheim, Germany, 2013, pp. 691–706. doi:10.1002/9783527673872.ch33.

[5] X. Rixhon, D. Tonelli, M. Colla, K. Verleysen, F. Contino, Integration of non-energy among the end-use demands of bottom-up whole energy system models, Frontiers in Energy Research 0 (2020) 1–10. doi:10.3389/FENRG.2022.904777.

[6] Fertilizers Europe, Overview 2021/22, Tech. rep. (2022).

[7] A. Valera-Medina, R. Banares-alcantara, Techno-economic Challenges of green ammonia as an energy carrier, Academic Press, 2021. doi:10.1016/c2019-0-01417-3.

[8] N. Salmon, R. Bañares-Alcántara, Green ammonia as a spatial energy vector: a review, Sustainable Energy & Fuels 5 (11) (2021) 2814–2839. doi:10.1039/d1se00345c.

[9] Belgium, Belgium's Integrated National Energy and Climate Plan [B] (2018).

[10] C. Peeters, Elia ' s view on Belgium ' s Energy Vision for 2050 (June) (2017) 1–22.
URL https://www.elia.be/{~}/media/files/Elia/publications-2/Rapports/Elia-view-on-Belgium-Energy-Vision-for-2050-EN.pdf

[11] G. Limpens, H. Jeanmart, Electricity storage needs for the energy transition: An EROI based analysis illustrated by the case of Belgium, Energy 152 (2018) 960–973. doi:10.1016/j.energy.2018.03.180.

[12] Executive Hydrogen Import Coalition, Shipping sun and wind to Belgium is key in climate neutral economy, Tech. rep.
URL https://beslissingenvlaamseregering.vlaanderen.be/document-view/5FAD539C20B6670008000274

[13] Institute for Sustainable Process Technology, ISPT, Power to Ammonia, Tech. rep., ISPT (2017).

[14] C. Philibert, Producing ammonia and fertilizers: new opportunities from renewables, IEA Report (2017) 1–6.

[15] M. Ozturk, I. Dincer, An integrated system for ammonia production from renewable hydrogen: A case study, International Journal of Hydrogen Energy 46 (8) (2021) 5918–5925. doi:10.1016/j.ijhydene.2019.12.127.

[16] C. Smith, A. K. Hill, L. Torrente-Murciano, Current and future role of Haber–Bosch ammonia in a carbon-free energy landscape, Energy & Environmental Science 13 (2) (2020) 331–344. doi:10.1039/c9ee02873k.

[17] R. Michael Nayak-Luke, R. Bañares-Alcántara, Techno-economic viability of islanded green ammonia as a carbon-free energy vector and as a substitute for conventional production, Cite this: Energy Environ. Sci 13 (2020) 2957. doi:10.1039/d0ee01707h.

[18] J. Armijo, C. Philibert, Flexible production of green hydrogen and ammonia from variable solar and wind energy: Case study of Chile and Argentina, International Journal of Hydrogen Energy 45 (3) (2020) 1541–1558.

[19] O. Osman, S. Sgouridis, A. Sleptchenko, Scaling the production of renewable ammonia: A techno-economic optimization applied in regions with high insolation, Journal of Cleaner Production 271 (2020) 121627. doi:10.1016/j.jclepro.2020.121627.

[20] J. Mitali, S. Dhinakaran, A. Mohamad, Energy storage systems: A review, Energy Storage and Saving (jul 2022). doi:10.1016/j.enss.2022.07.002.

[21] Ostuni, Method for load regulation of an ammonia plant (2008).

[22] I. I. Cheema, U. Krewer, Optimisation of the Autothermal NH3 Production Process for Power-to-Ammonia, Processes 8 (1) (2019) 38. doi:10.3390/pr8010038.

[23] I. I. Cheema, U. Krewer, Operating envelope of Haber–Bosch process design for power-to-ammonia, RSC Advances 8 (61) (2018) 34926–34936.

[24] S. Schulte Beerbühl, M. Fröhling, F. Schultmann, Combined scheduling and capacity planning of electricity-based ammonia production to integrate renewable energies, European Journal of Operational Research 241 (3) (2015) 851–862. doi:10.1016/J.EJOR.2014.08.039.

[25] R. Nayak-Luke, R. Bañares-Alcántara, I. Wilkinson, "Green" Ammonia: Impact of Renewable Energy Intermittency on Plant Sizing and Levelized Cost of Ammonia, Industrial & Engineering Chemistry Research 57 (43) (2018) 14607–14616.

[26] M. J. Palys, P. Daoutidis, Using hydrogen and ammonia for renewable energy storage: A geographically comprehensive techno-economic study, Computers and Chemical Engineering 136 (2020) 106785. doi:10.1016/j.compchemeng.2020.106785.

[27] I. Irena, Renewable power generation costs in 2017. report, International Renewable Energy Agency, Abu Dhabi (2018).

[28] Reuters, Yara says to halt Belgian fertiliser unit in the coming days (sep). URL https://rb.gy/yxjmph

[29] R. Freiberg, BASF closes ammonia production plant in Germany (mar 2023).
URL https://www.agriland.ie/farming-news/basf-closes-ammonia-production-plant-in-germany/

[30] R. Y. Rubinstein, D. P. Kroese, Simulation and the Monte Carlo method, Vol. 10, John Wiley & Sons, 2016.

[31] B. Sudret, Polynomial chaos expansions and stochastic finite element methods, Risk and reliability in geotechnical engineering (2014) 265–300.

[32] D. Coppitters, K. Verleysen, W. De Paepe, F. Contino, How can renewable hydrogen compete with diesel in public transport? Robust design optimization of a hydrogen refueling station under techno-economic and environmental uncertainty, Applied Energy 312 (2022) 118694.

[33] Z. Deng, X. Hu, X. Lin, Y. Che, L. Xu, W. Guo, Data-driven state of charge estimation for lithium-ion battery packs based on Gaussian process regression, Energy 205 (2020) 118000.

[34] B. Richard, C. Cremona, L. Adelaide, A response surface method based on support vector machines trained with an adaptive experimental design, Structural Safety 39 (2012) 14–21.

[35] H. Rabitz, Ö. F. Aliş, General foundations of high-dimensional model representations, Journal of Mathematical Chemistry 25 (2) (1999) 197–233.

[36] D. Coppitters, W. De Paepe, F. Contino, Robust design optimization of a photovoltaic-battery-heat pump system with thermal storage under aleatory and epistemic uncertainty, Energy 229 (2021) 120692. doi:10.1016/J.ENERGY.2021.120692.

[37] X. Rixhon, G. Limpens, D. Coppitters, H. Jeanmart, F. Contino, The Role of Electrofuels under Uncertainties for the Belgian Energy Transition, Energies 14 (13) (2021) 4027.

[38] B. Liu, Y. Wang, Energy system optimization under uncertainties: A comprehensive review, Towards Sustainable Chemical Processes (2020) 149–170.

[39] G. B. Dantzig, Linear programming under uncertainty, Management science 1 (3-4) (1955) 197–206.

[40] A. Zakaria, F. B. Ismail, M. H. Lipu, M. A. Hannan, Uncertainty models for stochastic optimization in renewable energy applications, Renewable Energy 145 (2020) 1543–1571.

[41] A. Ben-Tal, L. El Ghaoui, A. Nemirovski, Robust optimization, Princeton university press, 2009.

[42] Z. Kang, Robust design optimization of structures under uncertainties (2005).

[43] H. Yu, Reliability-based design optimization of structures: methodologies and applications to vibration control, Ph.D. thesis, Ecully, Ecole centrale de Lyon (2011).

[44] M. J. Palys, H. Wang, Q. Zhang, P. Daoutidis, Renewable ammonia for sustainable energy and agriculture: vision and systems engineering opportunities (2021).

[45] S. H. Lee, W. Chen, B. M. Kwak, Robust design with arbitrary distributions using Gauss-type quadrature formula, Structural and Multidisciplinary Optimization 39 (3) (2009) 227–243.

[46] V. Penadés-Plà, T. Garcia-Segura, V. Yepes, Robust design optimization for low-cost concrete box-girder bridge, Mathematics 8 (3) (2020) 398.

[47] T. Ghisu, J. P. Jarrett, G. T. Parks, Robust design optimization of airfoils with respect to ice accretion, Journal of Aircraft 48 (1) (2011) 287–304.

[48] W. Tian, Y. Heo, P. De Wilde, Z. Li, D. Yan, C. S. Park, X. Feng, G. Augenbroe, A review of uncertainty analysis in building energy assessment, Renewable and Sustainable Energy Reviews 93 (2018) 285–301.

[49] K. Verleysen, D. Coppitters, A. Parente, W. De Paepe, F. Contino, A. Parente, F. Contino, How can power-to-ammonia be robust? Optimization of an ammonia synthesis plant powered by a wind turbine considering operational uncertainties. 266 (2020) 117049.

[50] K. Verleysen, A. Parente, F. Contino, How does a resilient, flexible ammonia process look? Robust design optimization of a Haber-Bosch process with optimal dynamic control powered by wind, Proceedings of the Combustion Institute (jul 2022). doi:10.1016/J.PROCI.2022.06.027.

[51] D. Coppitters, W. De Paepe, F. Contino, Robust design optimization and stochastic performance analysis of a grid-connected photovoltaic system with battery storage and hydrogen storage, Energy 213 (2020) 118798. doi:10.1016/j.energy.2020.118798.

[52] Z. Cesaro, M. Ives, R. Nayak-Luke, M. Mason, R. Bañares-Alcántara, Ammonia to power: Forecasting the levelized cost of electricity from green ammonia in large-scale power plants, Applied Energy 282 (2021) 116009.

[53] A. Poullikkas, A comparative overview of large-scale battery systems for electricity storage, Renewable and Sustainable Energy Reviews 27 (2013) 778–788. doi:10.1016/J.RSER.2013.07.017.

[54] W. F. Holmgren, C. W. Hansen, M. A. Mikofski, pvlib python: a python package for modeling solar energy systems, The Journal of Open Source Software 3 (2018) 884.

[55] W. De Soto, S. A. Klein, W. A. Beckman, Improvement and validation of a model for photovoltaic array performance, Solar Energy 80 (1) (2006) 78–88.

[56] E. B. Iversen, J. M. Morales, J. K. Møller, H. Madsen, Probabilistic forecasts of solar irradiance using stochastic differential equations, Environmetrics 25 (3) (2014) 152–164.

[57] M. Kumar Panjwani, G. Bukshsh Narejo, Effect of Humidity on the Efficiency of Solar Cell (photovoltaic), International Journal of Engineering Research and General Science 2 (4) (2014) 499–503.

[58] Sunpower, X-Series residential solar panels: supplementary technical specifications.

[59] A. Buttler, H. Spliethoff, Current status of water electrolysis for energy storage, grid balancing and sector coupling via power-to-gas and power-to-liquids: A review, Renewable and Sustainable Energy Reviews 82 (2018) 2440–2454.

[60] Z. Abdin, C. J. Webb, E. M. Gray, Modelling and simulation of a proton exchange membrane (PEM) electrolyser cell, International Journal of Hydrogen Energy 40 (39) (2015) 13243–13257. doi:10.1016/j.ijhydene.2015.07.129.

[61] Y. Wang, J. Kowal, M. Leuthold, D. U. Sauer, Storage system of renewable energy generated hydrogen for chemical industry Selection and/or peer-review under responsibility of Canadian Hydrogen and Fuel Cell Association, Energy Procedia 29 (2012) 657–667. doi:10.1016/j.egypro.2012.09.076.

[62] M. Genovese, D. Blekhman, M. Dray, P. Fragiacomo, Hydrogen losses in fueling station operation, Journal of Cleaner Production 248 (2020) 119266. doi:10.1016/j.jclepro.2019.119266.

[63] A. Grinberg Dana, O. Elishav, A. Bardow, G. Shter, G. Grader, Nitrogen-Based Fuels: A Power-to-Fuel-to-Power Analysis (jul 2016). doi:10.1002/anie.201510618.

[64] M. J. Palys, A. Kuznetsov, J. Tallaksen, M. Reese, P. Daoutidis, A novel system for ammonia-based sustainable energy and agriculture: Concept and design optimization, Chemical Engineering and Processing - Process Intensification 140 (2019) 11–21. doi:10.1016/J.CEP.2019.04.005.

[65] M. Fasihi, R. Weiss, J. Savolainen, C. Breyer, Global potential of green ammonia based on hybrid PV-wind power plants, Applied Energy 294 (2021) 116170. doi:10.1016/j.apenergy.2020.116170.

[66] Elia, Our Infrastructure (2016).
URL https://www.elia.be/en/infrastructure-and-projects/our-infrastructure

[67] Aenert, Energy industry in Morocco (2022).
URL https://aenert.com/countries/africa/energy-industry-in-morocco/

[68] Ember, Carbon intensity of electricity, 2022 (2022).
URL https://ourworldindata.org/grapher/carbon-intensity-electricity

[69] X. Liu, A. Elgowainy, M. Wang, Life cycle energy use and greenhouse gas emissions of ammonia production from renewable resources and industrial by-products, Green Chemistry 22 (17) (2020) 5751–5761. doi:10.1039/D0GC02301A.

[70] N. Salmon, R. Bañares-Alcántara, Impact of grid connectivity on cost and location of green ammonia production: Australia as a case study, Energy & Environmental Science 14 (12) (2021) 6655–6671. doi:10.1039/D1EE02582A.

[71] K. Murugesan, V. Senniappan, Investigation of water management dynamics on the performance of a Ballard-Mark-V proton exchange membrane fuel cell stack system, Int. J. Electrochem. Sci 8 (2013) 7885–7904.

[72] Hellenic Shipping News, Sowing ZEEDS (Zero Emission Energy Distribution at Sea) of a new era | Hellenic Shipping News Worldwide (2019).
URL https://www.hellenicshippingnews.com/sowing-zeeds-zero-emissioni-energy-distribution-at-sea-of-a-new-era/

[73] Global Maritime Forum, How renewables can solve shipping's need for climate friendly fuel (2019).
URL https://www.globalmaritimeforum.org/news/how-renewables-can-solve-shippings-need-for-climate-friendly-fuel

[74] K. Kim, G. Roh, W. Kim, K. Chun, A Preliminary Study on an Alternative Ship Propulsion System Fueled by Ammonia: Environmental and Economic Assessments, Journal of Marine Science and Engineering 8 (3) (2020) 183. doi:10.3390/jmse8030183.

[75] M. Cames, N. Wissner, J. S. R. EV, perspectives. Öko-Institut, undefined 2021, Ammonia as a marine fuel, en.nabu.de.

[76] The Engineering Toolbox, Ammonia - Vapour Pressure at Gas-Liquid Equilibrium (2022).
URL https://www.engineeringtoolbox.com/ammonia-pressure-temperature-d_361.html

[77] shiptraffic.net, Sea distance calculator.
URL http://www.shiptraffic.net/2001/05/sea-distances-calculator.html

[78] Gelaro et al., renewables.ninja (2017).
URL doi:10.1175/JCLI-D-16-0758.1

[79] B. Zakeri, S. Syri, Electrical energy storage systems: A comparative life cycle cost analysis, Renewable and Sustainable Energy Reviews 42 (2015) 569–596. doi:10.1016/J.RSER.2014.10.011.

[80] D. Coppitters, P. Tsirikoglou, W. D. Paepe, K. Kyprianidis, A. Kalfas, F. Contino, RHEIA: Robust design optimization of renewable Hydrogen and dErIved energy cArrier systems, Journal of Open Source Software 7 (75) (2022) 4370. doi:10.21105/joss.04370.

[81] K. Deb, A. Pratap, S. Agarwal, T. Meyarivan, A fast and elitist multiobjective genetic algorithm: NSGA-II, IEEE Transactions on Evolutionary Computation 6 (2) (2002) 182–197.

[82] M. Stein, Large sample properties of simulations using latin hypercube sampling, Technometrics 29 (2) (1987) 143–151.

[83] D. Coppitters, Robust design optimization of hybrid renewable energy systems, Ph.D. thesis (2021).

[84] K. Deb, A. Pratap, S. Agarwal, T. Meyarivan, A fast and elitist multiobjective genetic algorithm: NSGA-II, IEEE Transactions on Evolutionary Computation 6 (2) (2002) 182–197. doi:10.1109/4235.996017.

[85] B. Sudret, Polynomial chaos expansions and stochastic finite-element methods, no. 2003, 2014.

[86] D. Coppitters, W. De Paepe, F. Contino, Surrogate-assisted robust design optimization and global sensitivity analysis of a directly coupled photovoltaic-electrolyzer system under techno-economic uncertainty, Applied Energy 248 (2019) 310–320.

[87] P. Lassák, J. Labovský, Ľ. Jelemenský, Influence of parameter uncertainty on modeling of industrial ammonia reactor for safety and operability analysis, Journal of Loss Prevention in the Process Industries 23 (2) (2010) 280–288.

[88] E. Torre, S. Marelli, P. Embrechts, B. Sudret, Data-driven polynomial chaos expansion for machine learning regression, Journal of Computational Physics 388 (2018) 601–623. arXiv:1808.03216, doi:10.1016/j.jcp.2019.03.039.

[89] S. Abraham, M. Raisee, G. Ghorbaniasl, F. Contino, C. Lacor, A robust and efficient stepwise regression method for building sparse polynomial chaos expansions, Journal of Computational Physics 332 (2017) 461–474.

[90] G. Blatman, B. Sudret, Efficient computation of global sensitivity indices using sparse polynomial chaos expansions, Reliability Engineering and System Safety 95 (11) (2010) 1216–1229. doi:10.1016/j.ress.2010.06.015.

[91] C. Fúnez Guerra, L. Reyes-Bozo, E. Vyhmeister, M. Jaén Caparrós, J. L. Salazar, C. Clemente-Jul, Technical-economic analysis for a green ammonia production plant in Chile and its subsequent transport to Japan, Renewable Energy 157 (2020) 404–414. doi:10.1016/J.RENENE.2020.05.041.

[92] J. Ikäheimo, J. Kiviluoma, R. Weiss, H. Holttinen, Power-to-ammonia in future North European 100 % renewable power and heat system, International Journal of Hydrogen Energy 43 (36) (2018) 17295–17308.

[93] J. Gorre, F. Ruoss, H. Karjunen, J. Schaffert, T. Tynjälä, Cost benefits of optimizing hydrogen storage and methanation capacities for Power-to-Gas plants in dynamic operation, Applied Energy 257 (2020) 113967. doi:10.1016/J.APENERGY.2019.113967.

[94] T. Huld, R. Müller, A. Gambardella, A new solar radiation database for estimating PV performance in Europe and Africa, Solar Energy 86 (6) (2012) 1803–1815.

[95] K. Verleysen, A. Parente, F. Contino, How sensitive is a dynamic ammonia synthesis process? Global sensitivity analysis of a dynamic Haber-Bosch process (for flexible seasonal energy storage), Energy 232 (2021) 121016.

[96] D. Frattini, G. Cinti, G. Bidini, U. Desideri, R. Cioffi, E. Jannelli, A system approach in energy evaluation of different renewable energies sources integration in ammonia production plants, Renewable Energy 99 (2016) 472–482.

[97] A. Araújo, S. Skogestad, Control structure design for the ammonia synthesis process, Computers & Chemical Engineering 32 (12) (2008) 2920–2932.

- A trade-off between energy efficiency and levelized cost is observed
- Robust design optimization considered 19 technical and economic uncertainties
- The power-to-ammonia plant in Belgium is more efficient but inhibits a higher levelized cost of ammonia
- Transporting ammonia from Morocco to Belgium is more economically beneficial but has a lower energy efficiency

Declaration of interests

☒ The authors declare that they have no known competing financial interests or personal relationships that could have appeared to influence the work reported in this paper.

☐The authors declare the following financial interests/personal relationships which may be considered as potential competing interests: